ACS Energy LETTERS

http://pubs.acs.org/journal/aelccp

LETTER

Multicomponent Approach for Stable Methylammonium-Free Tin−Lead Perovskite Solar Cells

Silver-Hamill Turren-Cruz,* Jorge Pascual, Shuaifeng Hu, Jesus Sanchez-Diaz, Sergio Galve-Lahoz, Wentao Liu, Wolfram Hempel, Vladimir S. Chirvony, Juan P. Martinez-Pastor, Pablo P. Boix, Atsushi Wakamiya,* and Iván Mora-Seró*

Cite This: *ACS Energy Lett.* 2024, 9, 432−441

Read Online

ACCESS | Metrics & More | Article Recommendations | Supporting Information

ABSTRACT: **Mixed tin−lead perovskites suffer from several degradation pathways that hinder their effective implementation in tandem photovoltaic technologies. The main challenge involves removing the thermally unstable methylammonium cation from the perovskite composition and simultaneously increasing the oxidation resistance of the tin-based material. This study employs a multicomponent approach to address these issues, developing methylammonium-free tin−lead perovskite solar cells with improved efficiency and stability. The incorporation of cations that tune precursor solution properties enhances the quality of MA-free perovskite films, while reducing agents and surface engineering techniques enhance robustness and carrier dynamics. Consequently, the methylammonium-free perovskite solar cells achieve over 22% efficiency and demonstrate significantly enhanced stability, with minimal losses after over 700 h of continuous operation under 1 sun illumination. This work evidences the potential of comprehensive strategies to process fragile materials, such as tin-containing perovskites, with improved quality and brings them closer to successful broad applications.**

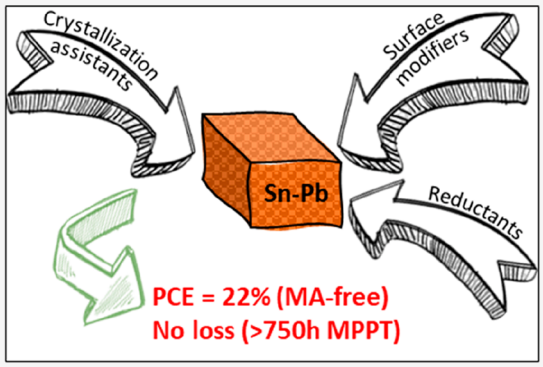

Mixed tin−lead (Sn−Pb) perovskites have recently gained significant attention in the field of photovoltaics owing to their narrow bandgaps, as low as ∼1.25 eV,[1,2] that allow them to play a critical role in the successful integration of double- or multiple-junction perovskite tandem photovoltaics (PVs).[3−8] For example, thanks to the comprehensive advancement of the field, double-junction all-perovskite tandems have reached power conversion efficiencies (PCEs) of over 29%.[9] This efficiency lies very close to the radiative limit of the single-junction solar cells at approximately 33%, while it is still far below their achievable maximum, ∼45%, based on the principle of detailed balance.[10]

One of the main limitations for the further development of the all-perovskite tandem PVs is the challenge of improving the narrow bandgap mixed Sn−Pb perovskite materials, and thus both their device efficiency and stability.[8,11,12] For improving the performance of perovskite solar cells (PSCs), one significant trend has been to tune perovskite compositions, most of the time by the rational combination of multiple cations at the A-site, such as methylammonium (MA), formamidinium (FA), guanidinium (Gua), and cesium cations.[4,13−17] FA is generally preferred as the main A-site cation in almost every high-efficiency PSC,[18] while another conventional cation MA suffers from gaseous degradation under elevated temperature.[19,20] Thus, for improving the device stability, it is of utmost importance to develop high-quality MA-free perovskites. The main problem with removing MA from these materials, including the case of mixed Sn−Pb perovskites, is the worsening of the crystallinity, which leads to films with a high density of defects and therefore limits the efficiency of the photovoltaic devices. This sums up the inherent instabilities that mixed Sn−Pb perovskites present in terms of Sn^{2+} oxidation into Sn^{4+}.[21] The community has proposed various methods to tackle these problems,[22] such as an alkylammonium pseudohalogen additive to improve the quality of MA-free mixed Sn−Pb films[23] or DMSO-free

Received: November 10, 2023
Revised: December 13, 2023
Accepted: December 29, 2023
Published: January 10, 2024

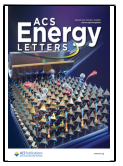

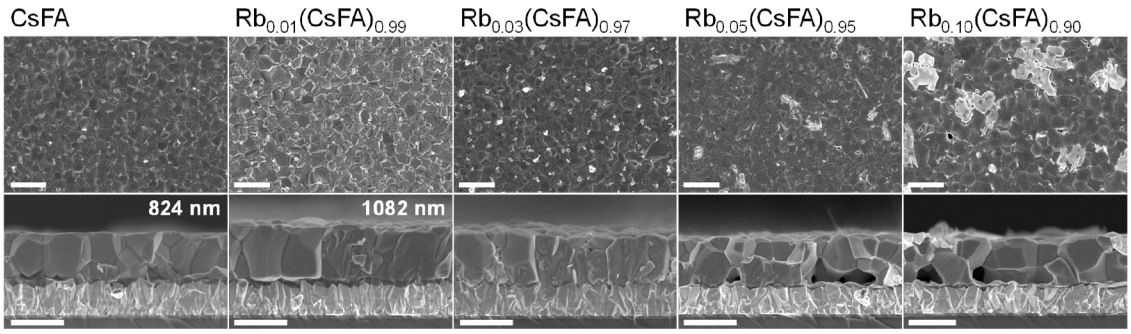

Figure 1. Top and cross-sectional SEM images for $Rb_x(CsFASnPbI_3)_{(100-x)}$ (x = 0, 1, 3, 5, and 10) perovskite films. The scale bar is 1 μm.

fabrication solvent(s) to reduce Sn^{2+} oxidation.[24] However, the complexity of these materials regarding their different degradation pathways demands comprehensive strategies that can address all of these issues collectively and not individually.

In this work, we present a multicomponent approach to simultaneously enhance the quality of MA-free mixed Sn/Pb thin films as well as their oxidation resistance. This holistic study unveils the separate and synergistic roles of different additives, rubidium (Rb) and dipropylammonium (Dip) cations for improving thin film crystallinity, and sodium borohydride ($NaBH_4$) as reducing agent, in order to increase the device stability. These compatible species allowed the fabrication of mixed Sn−Pb PSCs with efficiency values of over 22% and long-term operational stabilities of over 700 h with negligible efficiency loss. With this study, we highlight the potential of multicomponent strategies for particularly challenging materials mixed like Sn−Pb perovskites and contribute toward the future application in fabricating stable all-perovskite tandem PVs.

Different literature reports highlight the beneficial effect of the use of Rb cation in MA-free compositions for neat Pb[19] and mixed Sn−Pb perovskites.[23,25−27] Although its effectivity in reducing recombination losses has been discussed,[27] its full potential as well as the origin of its benefits in mixed Sn−Pb perovskite preparation remain unexplored, especially from the point of view of solution chemistry. Thus, we investigated a mixed Sn−Pb perovskite based on a precursor solution with the composition of $Cs_{0.2}FA_{0.8}Sn_{0.5}Pb_{0.5}I_3$, where we added rubidium iodide (RbI) from 1 to 10 mol % with the formula $Rb_x(Cs_{0.2}FA_{0.8}Sn_{0.5}Pb_{0.5}I_3)_{100-x}$ (x = 0, 1, 3, 5, and 10). For brevity, we respectively denoted these compositions as CsFA and Rb_xCsFA (where x is the relative percentage of added RbI). The preparation details are given in the Supporting Information.

Morphology of Perovskite Films. To gain an understanding of how the introduction of Rb cations affects the formation of thin films, we analyzed the morphological alterations by scanning electron microscopy (SEM). We used perovskite films containing CsFA and Rb_xCsFA. Top-view SEM images (Figure 1) revealed that increasing the Rb content leads to a slight enlargement in grain size (see Figures S1 for grain size distribution histograms). Specifically, the composition consisting solely of CsFA exhibited an average crystal size of ∼835 nm, uniformly distributed across the film surface. Upon adding 1 mol % of RbI, we observed an ∼50 nm increase in average grain size (∼882 nm). The introduction of 3 mol % of RbI led to a further increase, reaching ∼1000 nm. At this stage, Rb addition, however, started leading to agglomerations at the film surface. In the case of 5 and 10 mol % RbI, we observed an increase in the presence of these agglomerations. Interestingly, the films with 5 mol % RbI exhibited a decrease in grain size to ∼783 nm, while the 10 mol % one showed an increase to ∼936 nm, which is presumably caused by Rb-induced Ostwald ripening[28] or varied film growth dynamics with this certain big amount of Rb.

Figure 1 also includes cross-sectional SEM images of the perovskite films. In the CsFA case, we observed the grain boundaries at the cross section of the films. In contrast, the perovskite films prepared with the addition of 1 mol % RbI show a monolithic structure extending from the top to the bottom contact together with a notable increase in the thickness, from 824 to 1082 nm. With further addition of RbI at 3, 5, and 10 mol %, the fabricated films present a multigrain structure and voids form gradually at the buried interface. It is important to note that the appearance of pinholes and voids in the film is detrimental, increasing carrier recombination and acting as centers, where the material degradation initiates. These results evidence that too high concentrations of Rb cation in the film can disrupt the perovskite film morphology; however, reduced amounts as low as 1 mol % have a beneficial impact, greatly improving grain size and film thickness. Moreover, the increase in the thickness to over 1 μm is critical to maximizing the light absorption ability of the mixed Sn−Pb perovskite film due to its relatively lower absorption coefficient, especially at the band edge, compared with the neat Pb films.

We also compared our MA-free films with MA-containing reference and investigated the effect of 1 mol % RbI in the MA-containing perovskite films (see Figures S2 and S3). We denoted $Cs_{0.2}FA_{0.7}MA_{0.1}Sn_{0.5}Pb_{0.5}I_3$ and $Cs_{0.2}FA_{0.7}MA_{0.1}Sn_{0.5}Pb_{0.5}I_3$ + 1 mol % RbI perovskite films as CsFAMA and RbCsFAMA, respectively. First, we also observed that the addition of RbI causes a slight increase in the grain size of the MA-containing films; however, there was no significant change in the thickness of the MA-containing perovskite films. Addition of Rb does not change the film thickness in the case of MA-containing perovskite films (from 882 nm for CsFAMA to 891 nm for RbCsFAMA), in clear contrast with MA-free systems (from 824 nm for CsFA to 1082 nm for RbCsFA). Nevertheless, the addition of MA leads to a slight increase of film thickness (from 824 nm for CsFA to 882 nm for CsFAMA). These results show the ability of MA to increase the film thickness compared to CsFA, but in this case, Rb had no effect on this aspect when MA was present. This result suggests that although obviously different, MA and Rb cations may share, to some extent, a similar role in the solution-based crystallization process of FA-dominated perov-

https://doi.org/10.1021/acsenergylett.3c02426
ACS Energy Lett. 2024, 9, 432−441

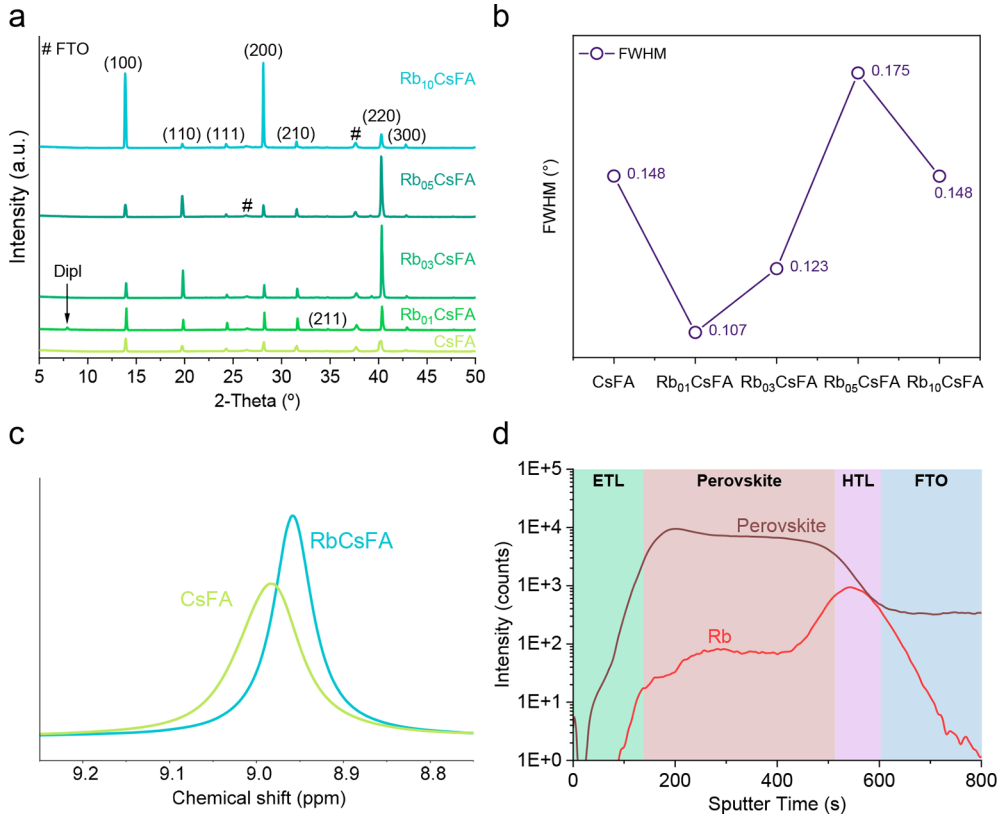

Figure 2. (a) X-ray diffraction (XRD) for MA-free CsFA-based perovskite films featuring varying concentrations of rubidium, (b) with the corresponding fwhm from 100 peak for CsFA, 1, 3, 5, and 10 mol % Rb. (c) ^{1}H NMR spectra at the FA N−H protons range with and without RbI addition for FAI solutions (in DMSO-d6:DMF-d7 at 1:3 volume ratio). (d) ToF-SIMS results of depth-dependent material content for Rb_{01}CsFA perovskite showing the distribution of perovskite material and Rb. The full compositional distribution description is given in Figure S9.

skite thin films. Thus, the more abundant MA would mask the influence of Rb on the film formation.

Film Crystallinity. To obtain information about the impact of Rb on the crystalline properties of the CsFA perovskite films, we conducted XRD measurements. We compared our MA-free compositions with the MA-based reference (see Figures 2a and S4). Contrary to CsFA films, these MA-containing films show the presence of PbI_2, whose peak is visible at 12.75°. Although some reports suggest that the presence of PbI_2 may not hinder the performance of the solar cells,[29] it is inevitably a source raising material degradation,[30] and therefore, we aim to reduce it. In addition to this, MA has low thermal stability, conditioning dramatically the long-term operational stability of the devices.[19] Thus, removing MA content from the perovskite material is necessary to ensure durable PSCs.[19] This process is not trivial, however, as MA-free perovskites typically suffer from lower film quality. In this case, it is not lattice instability, a common phenomenon occurring in FA-based neat Pb perovskites,[31] thanks to the stabilization from the replacement of Pb by Sn.[32] Instead, MA-free mixed Sn−Pb perovskites suffer from poorer morphology, caused by less controlled rates of nucleation and crystal growth.[33] The MA content in the precursor solution may hold an important role in the crystal growth mechanism, leading to more reproducible film fabrication with larger grains.[16] MA-containing samples present a (100) preferential orientation, as we can see in the high intensity ratio for (100) and (200) diffraction peaks, in comparison to the also present (110), (111), (210), and (220) reflections (see Figure S4a). After the MA content was removed from the mixed Sn−Pb perovskite composition (CsFA), we avoided the formation of PbI_2 (Figure 2a). In contrast, adding RbI to an MA-containing composition did not avoid PbI_2 formation (Figure S4b), and thus, this issue originates purely from MA introduction in the processing. With 1 mol % RbI, the (100) preferential orientation slightly increased. Interestingly, further increasing the RbI concentration promotes a (110) preferential orientation, except for the case of the sample with the highest Rb content (Figure 2a). A recent study showed the arising of the (110) peak when removing MA from the thin film.[34] Thus, MA-free compositions could potentially have a slight preference toward this orientation, which would then be exacerbated in the right conditions such as in the presence of Rb cation. It is also important to highlight the analysis of full width at half-maximum (fwhm) of the (100) diffraction peak, which presents a clear minimum for sample Rb_{01}CsFA, indicating that this sample presents the largest crystalline size. This sample does not present a clear preferential orientation, however, which several studies reported that it is not necessarily detrimental to the single junction and tandem device performance.[27,35−37] Consequently, considering the morphological and structural properties of the different analyzed films, Rb_{01}CsFA is the sample with the highest potential for the optimum PSC performance.

Properties of the Perovskite Precursor Solution. In order to understand the origin of the improved morphological and structural properties, we characterized the influence of RbI addition in the perovskite precursor solutions by NMR (using

https://doi.org/10.1021/acsenergylett.3c02426
ACS Energy Lett. 2024, 9, 432−441

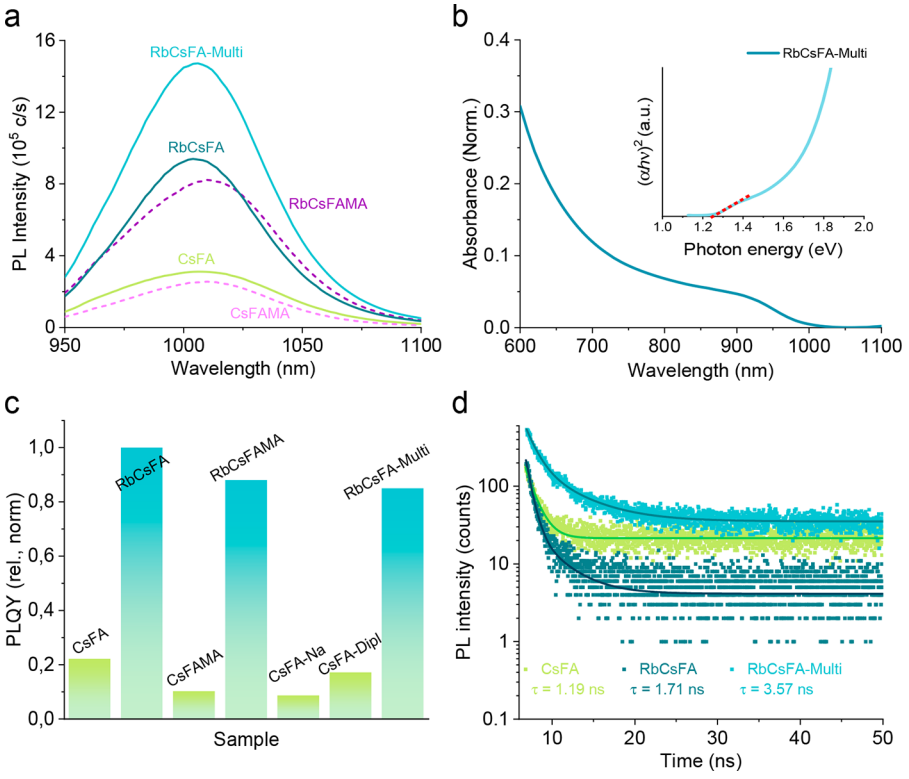

Figure 3. (a) PL data for the perovskite with different additives, (b) UV−vis absorption spectrum for RbCsFA-Multi film and Tauc plot (inset) resulting in a ∼1.21 eV absorption band edge energy, (c) PLQY for each additive, and (d) TRPL decay for perovskite films.

a Bruker 400 MHz Spectrometer at 298 K) and dynamic light scattering (DLS). First, in the ^{1}H NMR spectra of the different perovskite precursor solutions (see Figures 2c and S5a−d), we can identify the corresponding peaks for FAI protons. We additionally prepared only FAI as well as neat Sn and neat Pb perovskite solutions in order to identify a potential selectivity depending on the specific nature of the perovskite materials. The C−H signal is around 8.0 ppm, and the N−H protons appear in the 8.6−9.0 ppm range. The latter shows as a single signal for FAI and $FAPbI_3$ solutions, but as two split signals for $FASnPbI_3$ and $FASnI_3$ ones, suggesting that the presence of Sn-based precursors modifies the way the charge distributes around FA and the behavior of its aminic groups in solution. In a scenario in which the charge of the FA cation and thus its coordination to other components is unbalanced to one amine group, the signals at 8.7 and 9.0 ppm would respectively correspond to the more neutral and more charged amines, referred to as NH_2 and NH_2^+ in Table S1. When RbI is added on FAI solution, we observed a small decrease of 0.02 ppm in the chemical shift of the amine protons signal (see Figures 2c and S5a and Table S1). This shielding of the protons indicates a larger electronic density around them, which may originate from a higher coordination with the iodides in the iodidometalate $[MI_n]^{2-}$ species. This fact suggests that Rb cations may promote the degree of coordination of FA to perovskite and overall the prearrangement of perovskite precursors in solution and increasing colloidal stability, as previously discussed as a common nature of alkali cations.[38] This phenomenon would be explained by the ability of Rb cations to regulate the environment of halide anions, in this case, iodide, through coordinating them. This coordination may explain the formation of the increased repulsive interactions, increasing colloidal stability. For this particular reason, the role of alkali cations and, in general, A-site-like cations may actually vary depending on the nature of the anionic species in solution. This effect can have positive effects in thin film fabrication by facilitating a homogeneous nucleation. This shift was also present for the $FAPbI_3$ sample (see Figure S5b), with an additional slight shift of the C−H signal toward lower values. For the cases of $FASnPbI_3$ and $FASnI_3$ samples, where the NH protons split into two different signals, after RbI addition, we only observed a small shift of 0.01 ppm for the most deshielded signal at ∼8.9 ppm, while the more shielded one remained invariable at ∼8.7 ppm. This reveals that the Rb cation has an influence in the environment and coordination by FA and that it is dominated by the more deshielded amine. According to these results summarized in Table S1, this shift is consistent and present in all FAI and Sn or Pb perovskite samples after the addition of RbI, confirming the direct influence of Rb on the coordination of FA within the perovskite. As stated before, though the shift of 0.02 ppm is small, it suggests that Rb cation addition can influence and interact with prearranged perovskite precursors in solution. Meanwhile, DLS results did not show any significant variation in the distribution of colloidal size in perovskite precursor solutions with different RbI amounts, suggesting that the Rb cation would not impact strongly on the as-prepared precursor solutions but would influence latter stages of the crystallization through its ability to interact with different perovskite components (see Figure S6).

Multicomponent Approach. All of these results suggest that rubidium cation opens the door to a more controlled crystallization process and better film morphology, a critical advancement for mixed Sn−Pb perovskite materials and particularly for MA-free compositions. However, the enhancement of the perovskite optoelectronic properties requires the

https://doi.org/10.1021/acsenergylett.3c02426
ACS Energy Lett. 2024, 9, 432−441

integration of additional additives to comprehensively address all challenges posed by the nature of MA-free Sn−Pb materials. Here, we introduced dipropylammonium iodide (DipI), where Dip^+ is an organic bulky cation additive that can be used to improve the performance and stability of PSCs. Dip^+ has larger size and a longer alkyl chains than the commonly used MA and FA cations,[39,40] which can affect the crystal growth, morphology, and electronic properties of the perovskite layer.[39] Particularly, the addition of Dip^+ induces the formation of slightly larger crystals with more defined shapes and lower surface roughness compared to the pristine films. Simultaneously, we also included sodium borohydride ($NaBH_4$) to counteract the oxidation of Sn^{2+} into Sn^{4+} and the potentially formed I_2[40] that can degrade the perovskite layer.[41]

The multicomponent combination of these two additives DipI and $NaBH_4$ together with RbI, denoted as RbCsFA-Multi, has no negative impact on the morphology of CsFA perovskite, as evidenced in Figure S7, where we observe perovskite structures characterized by large grains and a relatively uniform surface. Furthermore, separate XRD analyses of this perovskite film revealed an influence of each additive, individually or collectively, on the perovskite preferential orientation (Figure S8a). However, the use of the additives in Rb_{01}CsFA does not decrease the crystallite size (see Figure S8b).

Compositional Distributions. After confirming the involvement of Rb in the crystallization process of MA-free Sn−Pb perovskites, we looked for its spatial distribution within the film and assessed any potential depth-dependent characteristics. We utilized time-of-flight secondary ion mass spectrometry (ToF-SIMS) to analyze perovskite films containing all additives. Our findings revealed a uniform distribution of all perovskite constituents throughout the thin film (see Figure S9), with a slight predilection for Rb at the lower interface (see Figure 2d). Furthermore, we observed a preference for Na at the bottom interface and DipI presence at the top interface (see Figure S9). The similar behavior of Na and Rb cations in this aspect highlights the similar nature of alkali cations and probably a comparable role in the crystallization process, as discussed in a previous work.[38] Moreover, aside from assisting crystallization for larger and denser grain formation, Dip^+ and Na^+ cations may function as potential defect mitigators, with a preference for localization at the interfaces, encompassing buried surfaces, top layers, and grain boundaries. These materials can react with surface defects or dangling bonds on perovskite crystals, reducing the density of trap states within the material.

Photophysical Properties. For effective charge extraction, high-quality perovskite films with long charge carrier lifetimes are necessary. We evaluated the improvements in the carrier dynamics using steady-state photoluminescence (PL) and time-resolved PL (TRPL). For PL analysis, all the different perovskite films analyzed in previous sections were deposited on glass. The perovskite films were excited from the top surface of the perovskite film. In each condition, a single PL peak around 1008 nm was observed, with PL lifetimes on the order of a few nanoseconds. Note that the PL spectrum is slightly blue-shifted for Rb-contained films (see Figure 3a). Comparison of CsFA-based samples is in Figure S10a. One of the possible origins for such small blue shift of bandgap increase (∼10 meV) can be an Rb-derived compositional deviation at the film surface. We showed previously how introduction of Rb can affect the composition of the crystal in the bulk.[19,42,43] These assumptions are reasonable, considering that the surface quality of the films without Rb is likely somewhat worse than the treated materials. One more possible explanation of PL blue shift for Rb-containing samples is that these samples are less scattering (due to their better optical quality) and thus less subjected to the PL red shift because of multiple scattering and reabsorption (photon recycling effect). We also observed an increase of the PL intensity for all Rb-containing samples, with and without MA (see Figure 3a). Absorption onset does not show any shifting for any of the samples, but it is possible to see and increment on the absorption edge; see Figure S10b, mostly due to the higher thickness of the films with Rb. Moreover, in Figure 3b, the Tauc plot indicates an absorption band edge energy of ∼1.21 eV for the RbCsFA-Multi sample, confirming that this material has the ideal narrow bandgap for application on all-perovskite tandem solar cells. On the other hand, we observed an increase in intensity for all Rb-containing samples, with and without MA (Figure 3a). We evaluated also relative photoluminescence quantum yield (PLQY) for all samples (see the method for the evaluation in the Supporting Information), observing a significant increase of 4-fold for every perovskite containing Rb cation (see Figure 3c and Table S2). Furthermore, the TRPL spectra agree well with the observed trend in the PLQY, because the PL decay time increases from 1.19 ns for CsFA to 1.71 ns for the RbCsFA films. Particularly interesting is the case of RbCsFA-Multi films, for which an increase to 3.57 ns is observed (see Figure 3d). These results point to a decrease of nonradiative recombination rate. Moreover, this result confirms that RbI and DipI additives reduce the nonradiative recombination rate in the perovskite film, also on films containing MA (see Table S2 and Figure S11).

Device Performance. We statistically evaluated the photovoltaic potential of the FTO/PEDOT:PSS/perovskite/C_{60}/BCP/Ag stack. In Figure S12 is reported the observed significant improvement in the average J_{SC} of CsFA (26.59 mA cm^{-2}) after Rb addition (31.23 mA cm^{-2}). V_{OC} gradually decreased with increasing amounts of Rb, from 0.75 to 0.38 V. The average fill factor (FF) increased from 64 to 70%, finally translating into an improved average PCE from 12.15 to 13.24% when comparing CsFA reference with Rb_{01}CsFA samples. Most importantly, the Rb improves the reproducibility as particularly noticeable in the FF. Incorporating long organic cations like DipI, which do not easily fit into the octahedral structure, serves as a "barrier" and effectively "caps" the three-dimensional perovskite, leading to the formation of a layered structure.[44] The materials under investigation share a common structural formula represented as $Dip_2FA_{n-1}(Sn_{0.5}Pb_{0.5})_nI_{3n+1}$.[39] Within this structural representation of layered perovskites, the variable "*n*" denotes the dimensions of the two-dimensional slabs. In this structural formula for the layered perovskites, *n* indicates the size of the two-dimensional slabs. We then prepared PSCs with varying concentrations of DipI for nominal n = 0, 10, 20, 30, 40, and 50 in order to find the best *n*. In this case, n = 30 yielded the best performance (see Figure S13). After identifying the optimal conditions for Rb and DipI to enhance the results, we evaluated RbCsFA-Multi at varying molarities. As we show in Figure S14, perovskite solution concentration had an impact on the final device performance, where we found the optimal molarity of 1.9 M for the total solution (see more details in the Supporting Information). The photovoltaic characteristics of the best PSCs for CsFA and RbCsFA-Multi are plotted in

https://doi.org/10.1021/acsenergylett.3c02426
ACS Energy Lett. 2024, 9, 432−441

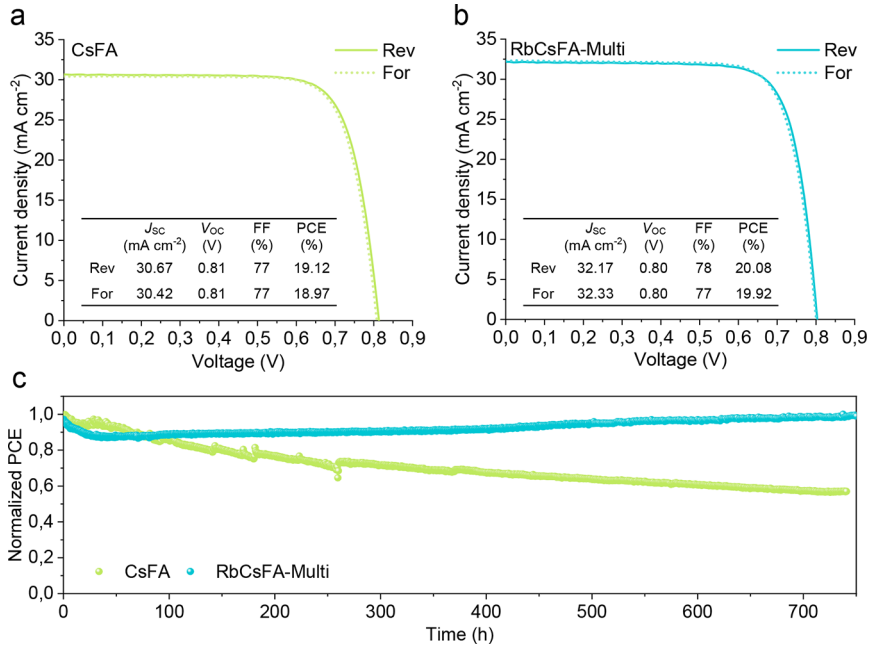

Figure 4. Best performing device $J-V$ and stability. (a) $J-V$ curves of the CsFA device, (b) $J-V$ curves of the RbCsFA-Multi device, and (c) MPP measurement of control and target devices aged for >700 h after encapsulation.

Figure 4a,b. The Rb-free control device presented a PCE of 19.12%, where we noticed a particularly low current density. Upon addition of 1% Rb into the mixed perovskite RbCsFA-Multi, the J_{SC} increased from 30.67 to 32.17 mA cm^{-2}. Consequently, the multicomponent devices showed improved efficiencies of up to 20.08% in comparison to the other compositions. The most significant improvements were in the J_{SC} and FF (see Figure S15). The materials showed improvements also when separately added, such as the FF increase for CsFA-DipI, or the higher J_{sc} for CsFA-Na and RbCsFA, though with lower reproducibility.

Beyond PCE, stability is one of the main challenges for future PSC commercialization. However, relatively few stability data sets exist for the Sn−Pb PSCs. To analyze the impact of our multicomponent strategy on device stability, we tracked CsFA and RbCsFA-Multi devices at the maximum-power point (MPP) at room temperature for 750 h under continuous illumination (100 mW cm^{-2}, AM1.5G) at a constantly applied voltage of 0.67 for CsFA and 0.68 V for RbCsFA-Multi devices, with encapsulation of 2 μm SiO_x at 60% RH.[45] See Figure S16 and Tables S3 and S4 for the MPP tracking analysis during the measurement time. Figure 4c shows that the CsFA device performance deteriorates fast, starting at 19.50% and finishing at 10.54% PCE after 750 h, with a T_{80} of 140 h. Following the initial component, there is approximately a 30% efficiency loss. The initial efficiency is sustained at 100% for several hours before a gradual decline sets in, reaching values of 98%, 95%, and 90% of the initial PCE after 10, 20, and 30 h, respectively. Beyond the 30 h mark, a more rapid performance decrease occurs, delineating two distinct efficiency drop regions: (1) a gradual PCE decrease linked to the loss of fill factor (FF) due to device heating (temperature reaching 60 °C due to lamp heat radiation) and (2) a swift reduction in PCE attributed to the oxidative degradation of $FASnI_3$. Regardless, the evident correlation between the loss of PCE and the decline in current density (Figure S16b) suggests that both phenomena—FF loss due to heating and oxidative degradation of $FASnI_3$—temporarily coexist during the initial 5 h under the measuring conditions. Nevertheless, the RbCsFA-Multi devices exhibited markedly enhanced stability performance. The absolute PCE initiates at 20.64%, experiences a modest drop of approximately 13% after the initial 30 h, and subsequently demonstrates a sustained recovery in the long-term component, stabilizing at a final PCE of 20.21%. While both devices initially followed a similar trend, the RbCsFA-Multi device began to degrade within the first 30 h, resulting in a 13% loss of the initial PCE. In contrast, the PCE of the RbCsFA-Multi device progressively increased, reaching up to 94% of the initial PCE after 700 h of light exposure (Figure 4c). Similar trends were observed for the RbCsFA-Multi devices, albeit at slightly different rates. The decline in PCE was predominantly attributed to fill factor (FF) loss. Notably, there were insignificant variations in V_{oc} and J_{sc} (Figure S16c). Although the positive impact of light-soaking in Sn-based solar cells has been reported previously,[46] its exact origin remains unclear.

We also carried out XRD analyses of films after thermal stress at 130 °C for 3 h inside the glovebox under N_2 (see Figures S17 and S18), in order to see the impact on thermal stability of the additives and the MA content. All samples exhibited a reduction of diffraction peak intensities after thermal stress, which were higher for samples without Rb. RbCsFA-Multi presented significantly the best thermal stability with practically no decrease on diffraction peak intensity (Figure S18). This analysis is a clear motivation for avoiding MA and using original additive combinations in future compositions for ensuring long-term stability especially under thermal stress. These stability data highlight the significance of multicomponent strategies to comprehensively address degradation sources and enhance long-term stability of Sn−Pb PSCs.

We included a surface treatment of the perovskite layer with 4-fluoro-phenylethylammonium chloride (4FPEACl), as a further step to increase device PCE. In recent times, significant advancements have been achieved in optimizing perovskite

https://doi.org/10.1021/acsenergylett.3c02426
ACS Energy Lett. 2024, 9, 432−441

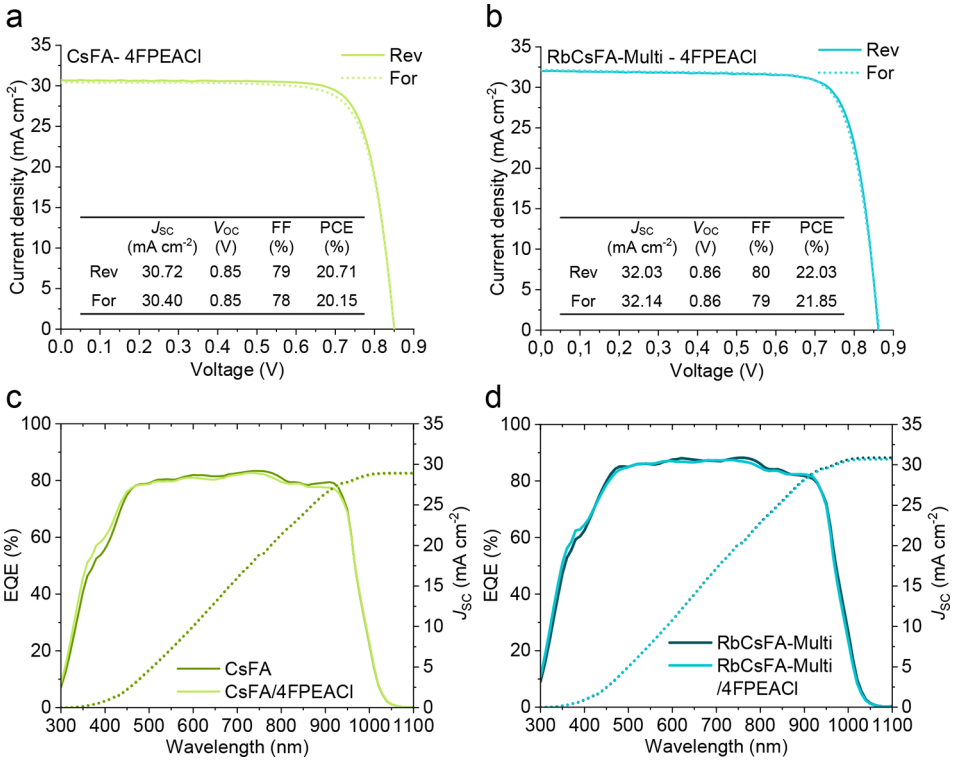

Figure 5. $J-V$ curves of the best performing devices with interfacial engineering. (a) $J-V$ curve of CsFA device with 4FPEACl, (b) $J-V$ curve of RbCsFA-Multi device with 4FPEACl, and (c and d) the corresponding EQE spectra.

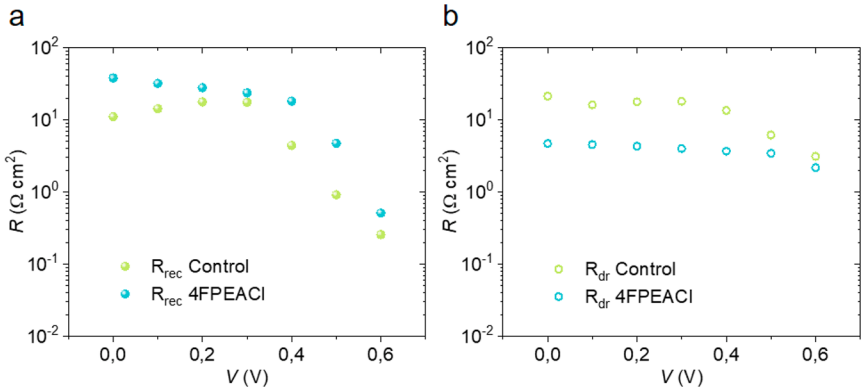

Figure 6. (a) Recombination resistance and (b) ionic-related resistance extracted from impedance spectroscopy for the RbCsFA-Multi devices with and without 4FPEACl surface modification.

interfaces by employing an ammonium ligand-composed buffer layer. These layers play a crucial role in passivating the perovskite, diminishing recombination, alleviating the adverse effects of pinholes, and preventing the migration of metal electrodes at elevated temperatures.[47] This approach has been applied at the perovskite/electron transporting layer (ETL) interface with organic cations like phenethylammonium iodide, ethylenediammonium, and 4-fluoro-phenylethylammonium iodide (4FPEAI).[37,48−50] Therefore, we explored the potential of surface engineering for the perovskite/ETL interface by using our optimized films.

Devices modified with FPEACl showed significantly improved efficiency (Figures 5). The top-performing devices with 4FPEACl modification delivered an efficiency of 20.71% for CsFA and 22.03% for RbCsFA-Multi (see Figure 5a,b, respectively). The J_{SC} of 30.71 mA cm^{-2} for CsFA and 32.03 mA cm^{-2} for RbCsFA-Multi are in good agreement with those values integrated from the EQE spectra of 28.95 and 31.06 mA cm^{-2} (see Figure 5c,d, respectively). Notably, the voltage drastically increased upon the insertion of 4FPEACl. The 22.03% PCE champion device exhibited a V_{OC} of 0.86 V and a FF of 80%. Moreover, in Figure S19 we see that devices with a 4FPEACl interlayer show some of the highest PCE and exhibit more reproducible device parameters, especially in terms of V_{oc} and FF, and these results highlight the potential of interfacial engineering and the compatibility with multicomponent strategies for combined benefits.

To rationalize the performance differences after 4FPEACl modification of the RbCsFA-Multi devices, we measured the devices by impedance spectroscopy under 1 sun illumination. The spectra were fitted using an equivalent circuit previously presented,[51] with a series resistance (R_s) to model the transport resistance of cables and contacts, a recombination resistance (R_{rec}) to account for the charge recombination

https://doi.org/10.1021/acsenergylett.3c02426
ACS Energy Lett. 2024, 9, 432−441

considering negligible the transport resistance at perovskite layer, a geometric capacitance (C_g) for the whole device, and a parallel branch where a resistor (R_{dr}) and a capacitor (C_{dr}) model the ionic phenomena. The evolution of the parameters across the relevant bias region displays a significantly higher R_{rec} for the 4FPEACl-modified devices (Figure 6a), which indicates a lower recombination rate and explains its improved V_{OC}. The geometric capacitance presents equivalent values for both devices (Figure S20), as expected for devices with the same thickness. Interestingly, the 4FPEACl device also displays lower R_{dr} and marginally higher C_{dr} (see Figures 6b and S20, respectively). This fact indicates, in combination, a slightly lower vacancy concentration and higher diffusion coefficient for the ions in the control sample.[52] These results suggest that 4FPEACl may act as a surface passivation agent, mitigating surface defects and traps in the perovskite film. This can enhance the charge carrier lifetime and reduce recombination, leading to an improved overall device performance. Liu et al. recently showed that 4F-PEACl acts as a positive dipole layer to reduce recombination losses and that it has an impact on the barrier for carrier transport.[53] Accordingly, the V_{OC} and FF of our devices were positively influenced by the insertion of this surface modifier.

Narrow bandgap mixed Sn−Pb perovskites for tandem technologies face complex degradation processes that require innovative solutions. In this work, we proved the potential of multicomponent methodologies to address them in a comprehensive manner. A carefully optimized combination of organic and inorganic compounds led to greatly enhanced morphological, structural, and optoelectronic properties of MA-free Sn−Pb perovskite films. Remarkably, even a minimal 1 mol % addition of RbI to the precursor solution resulted in improved film morphology and thickness. We observed the critical role of the Rb cation in manipulating precursor solution characteristics. Moreover, when combined with other additives such as $NaBH_4$ and DipI, the films presented enhanced exciton recombination lifetimes, and the use of 4FPEACl as an interlayer material substantially increased film mobility. We believe this enhancement plays a crucial role in recombination suppression. The systematic use of multicomponent additives consistently resulted in improved optical (or carrier-recombination) properties, higher V_{OC} and FF, and negligible loss of photovoltaic efficiency under MPPT measurement for over 700 h under N_2 atmosphere. Our work represents a significant advancement in comprehending and improving the quality of MA-free Sn−Pb perovskites, bringing them a step closer to the development of stable and efficient all-perovskite tandem solar cells in the near future.

■ ASSOCIATED CONTENT

Supporting Information

The Supporting Information is available free of charge at https://pubs.acs.org/doi/10.1021/acsenergylett.3c02426.

Full experimental details, including materials, device fabrication, measurement, and analysis; Figures S1−S20, showing grain size distribution histograms, SEM and XRD of the perovskite films fabricated, ^{1}H NMR spectra of FA in perovskite precursor solutions and DLS with and without RbI addition, ToF-SIMS measurements of the RbCsFA-Multi perovskite film, J−V curves and extended discussion of steady-state PL and TRPL of the perovskite films with different composition, box plots showing the distribution of the photovoltaic parameters for the solar cells, MPPT of the PSCs, and the geometric capacitance C_g and marginally higher C_{dr} (PDF)

■ AUTHOR INFORMATION

Corresponding Authors

Silver-Hamill Turren-Cruz − *Institute of Advanced Materials (INAM), University Jaume I, 12071 Castellón de la Plana, Spain; Institute for Chemical Research, Kyoto University, Kyoto 611-0011, Japan; Department of Physical Chemistry, Polish Academy of Sciences, Warsaw 01-224, Poland;* orcid.org/0000-0003-3191-6188; Email: silver.turren@gmail.com

Atsushi Wakamiya − *Institute for Chemical Research, Kyoto University, Kyoto 611-0011, Japan;* orcid.org/0000-0003-1430-0947; Email: wakamiya@scl.kyoto-u.ac.jp

Iván Mora-Seró − *Institute of Advanced Materials (INAM), University Jaume I, 12071 Castellón de la Plana, Spain;* orcid.org/0000-0003-2508-0994; Email: sero@uji.es

Authors

Jorge Pascual − *Institute for Chemical Research, Kyoto University, Kyoto 611-0011, Japan; Polymat, University of the Basque Country UPV/EHU, 20018 Donostia-San Sebastian, Spain*

Shuaifeng Hu − *Institute for Chemical Research, Kyoto University, Kyoto 611-0011, Japan; Clarendon Laboratory, Department of Physics, University of Oxford, Oxford OX1 3PU, U.K.;* orcid.org/0000-0003-1312-075X

Jesus Sanchez-Diaz − *Institute of Advanced Materials (INAM), University Jaume I, 12071 Castellón de la Plana, Spain*

Sergio Galve-Lahoz − *Institute of Advanced Materials (INAM), University Jaume I, 12071 Castellón de la Plana, Spain; Polymat, University of the Basque Country UPV/EHU, 20018 Donostia-San Sebastian, Spain*

Wentao Liu − *Institute for Chemical Research, Kyoto University, Kyoto 611-0011, Japan*

Wolfram Hempel − *Zentrum für Sonnenenergie- und Wasserstoff-Forschung Baden-Württemberg (ZSW), 70563 Stuttgart, Germany*

Vladimir S. Chirvony − *Instituto de Ciencia de los Materiales (ICMUV), Universidad de Valencia, E-46980 Paterna, Spain;* orcid.org/0000-0003-4121-9773

Juan P. Martinez-Pastor − *Instituto de Ciencia de los Materiales (ICMUV), Universidad de Valencia, E-46980 Paterna, Spain*

Pablo P. Boix − *Instituto de Ciencia de los Materiales (ICMUV), Universidad de Valencia, E-46980 Paterna, Spain;* orcid.org/0000-0001-9518-7549

Complete contact information is available at: https://pubs.acs.org/10.1021/acsenergylett.3c02426

Notes

The authors declare no competing financial interest.

■ ACKNOWLEDGMENTS

S.-H.T.-C. would like to thank the Ministry of Science and Innovation of Spain (postdoctoral contract Juan de la Cierva Formación FJC2019-041835-I), Generalitat Valenciana under BEST project (CIBEST/2021/234) and POLONES BIS 1 (DEC-2021/43/P/ST5/01780) for the financial support

during this work. J.P. acknowledges DonostiaINN for a postdoctoral fellowship. I.M.-S. and P.P.B. want to acknowledge funding support of Ministry of Science and Innovation of Spain under PERIPHERAL (PID2020-120484RB project), Step-Up (TED2021-131600B-C31 and TED2021-131600B-C32, respectively). S.H. acknowledges the financial support from JSPS for a Research Fellowship for Young Scientists (21J14762) and the Chinese Scholarship Council (CSC). I.M.-S. acknowledges the funding from University Jaume I under the project Sn-flex (22I586), and A.W. acknowledges the financial support from JST-Mirai Program (JPMJMI22E2), NEDO, Grant-in-Aid for Scientific Research (A) (21H04699), the International Collaborative Research Program of ICR, Kyoto University, ICR Grants for Promoting Integrated Research, Kyoto University, grants for the Integrated Research Consortium on Chemical Sciences.

REFERENCES

(1) Hao, F.; Stoumpos, C. C.; Cao, D. H.; Chang, R. P. H.; Kanatzidis, M. G. Lead-free solid-state organic−inorganic halide perovskite solar cells. *Nat. Photonics* **2014**, *8*, 489−494.

(2) Klug, M. T.; Milot, R. L.; Patel, J. B.; Green, T.; Sansom, H. C.; Farrar, M. D.; Ramadan, A. J.; Martani, S.; Wang, Z. P.; Wenger, B.; et al. Metal composition influences optoelectronic quality in mixed-metal lead-tin triiodide perovskite solar absorbers. *Energy Environ. Sci.* **2020**, *13* (6), 1776−1787.

(3) McMeekin, D. P.; Sadoughi, G.; Rehman, W.; Eperon, G. E.; Saliba, M.; Horantner, M. T.; Haghighirad, A.; Sakai, N.; Korte, L.; Rech, B.; et al. A mixed-cation lead mixed-halide perovskite absorber for tandem solar cells. *Science* **2016**, *351* (6269), 151−155. From NLM PubMed-not-MEDLINE

(4) Eperon, G. E.; Leijtens, T.; Bush, K. A.; Green, T.; Tse-Wei Wang, J.; McMeekin, D. P.; Volonakis, G.; Milot, R. L.; Slotcavage, D. J.; Belisle, R. Perovskite-perovskite tandem photovoltaics with ideal bandgaps. *ArXiv* **2016**, 1608.03920.

(5) McMeekin, D. P.; Mahesh, S.; Noel, N. K.; Klug, M. T.; Lim, J.; Warby, J. H.; Ball, J. M.; Herz, L. M.; Johnston, M. B.; Snaith, H. J. Solution-Processed All-Perovskite Multi-junction Solar Cells. *Joule* **2019**, *3* (2), 387−401.

(6) Wang, J.; Zardetto, V.; Datta, K.; Zhang, D.; Wienk, M. M.; Janssen, R. A. J. 16.8% Monolithic all-perovskite triple-junction solar cells via a universal two-step solution process. *Nat. Commun.* **2020**, *11* (1), 5254. From NLM PubMed-not-MEDLINE

(7) Hörantner, M. T.; Leijtens, T.; Ziffer, M. E.; Eperon, G. E.; Christoforo, M. G.; McGehee, M. D.; Snaith, H. J. The Potential of Multijunction Perovskite Solar Cells. *ACS Energy Letters* **2017**, *2* (10), 2506−2513.

(8) Wang, R.; Huang, T. Y.; Xue, J. J.; Tong, J. H.; Zhu, K.; Yang, Y. Prospects for metal halide perovskite-based tandem solar cells. *Nat. Photonics* **2021**, *15* (6), 411−425.

(9) Green, M. A.; Dunlop, E. D.; Yoshita, M.; Kopidakis, N.; Bothe, K.; Siefer, G.; Hao, X. J. Solar cell efficiency tables (version 62). *Prog. Photovoltaics* **2023**, *31* (7), 651−663.

(10) Shockley, W.; Queisser, H. J. Detailed Balance Limit of Efficiency of p-n Junction Solar Cells. *J. Appl. Phys.* **1961**, *32* (3), 510−519.

(11) Gu, S.; Lin, R.; Han, Q.; Gao, Y.; Tan, H.; Zhu, J. Tin and Mixed Lead-Tin Halide Perovskite Solar Cells: Progress and their Application in Tandem Solar Cells. *Adv. Mater.* **2020**, *32* (27), No. e1907392. From NLM PubMed-not-MEDLINE

(12) Zheng, X. P.; Alsalloum, A. Y.; Hou, Y.; Sargent, E. H.; Bakr, O. M. All-Perovskite Tandem Solar Cells: A Roadmap to Uniting High Efficiency with High Stability. *Accounts of Materials Research* **2020**, *1* (1), 63−76.

(13) Liu, X.; Yang, Z. B.; Chueh, C. C.; Rajagopal, A.; Williams, S. T.; Sun, Y.; Jen, A. K. Y. Improved efficiency and stability of Pb-Sn binary perovskite solar cells by Cs substitution. *J. Mater. Chem. A* **2016**, *4* (46), 17939−17945.

(14) Zong, Y.; Wang, N.; Zhang, L.; Ju, M. G.; Zeng, X. C.; Sun, X. W.; Zhou, Y.; Padture, N. P. Homogenous Alloys of Formamidinium Lead Triiodide and Cesium Tin Triiodide for Efficient Ideal-Bandgap Perovskite Solar Cells. *Angew. Chem., Int. Ed. Engl.* **2017**, *56* (41), 12658−12662. From NLM PubMed-not-MEDLINE

(15) Prasanna, R.; Gold-Parker, A.; Leijtens, T.; Conings, B.; Babayigit, A.; Boyen, H. G.; Toney, M. F.; McGehee, M. D. Band Gap Tuning via Lattice Contraction and Octahedral Tilting in Perovskite Materials for Photovoltaics. *J. Am. Chem. Soc.* **2017**, *139* (32), 11117−11124. From NLM PubMed-not-MEDLINE

(16) Saliba, M.; Matsui, T.; Seo, J. Y.; Domanski, K.; Correa-Baena, J. P.; Nazeeruddin, M. K.; Zakeeruddin, S. M.; Tress, W.; Abate, A.; Hagfeldt, A.; Gratzel, M. Cesium-containing triple cation perovskite solar cells: improved stability, reproducibility and high efficiency. *Energy Environ. Sci.* **2016**, *9* (6), 1989−1997. From NLM PubMed-not-MEDLINE

(17) Tong, J.; Song, Z.; Kim, D. H.; Chen, X.; Chen, C.; Palmstrom, A. F.; Ndione, P. F.; Reese, M. O.; Dunfield, S. P.; Reid, O. G.; et al. Carrier lifetimes of > 1 mus in Sn-Pb perovskites enable efficient all-perovskite tandem solar cells. *Science* **2019**, *364* (6439), 475−479. From NLM PubMed-not-MEDLINE

(18) Jesper Jacobsson, T.; Correa-Baena, J.-P.; Pazoki, M.; Saliba, M.; Schenk, K.; Grätzel, M.; Hagfeldt, A. Exploration of the compositional space for mixed lead halogen perovskites for high efficiency solar cells. *Energy Environ. Sci.* **2016**, *9* (5), 1706−1724.

(19) Turren-Cruz, S. H.; Hagfeldt, A.; Saliba, M. Methylammonium-free, high-performance, and stable perovskite solar cells on a planar architecture. *Science* **2018**, *362* (6413), 449−453. From NLM PubMed-not-MEDLINE

(20) Juarez-Perez, E. J.; Ono, L. K.; Maeda, M.; Jiang, Y.; Hawash, Z.; Qi, Y. B. Photodecomposition and thermal decomposition in methylammonium halide lead perovskites and inferred design principles to increase photovoltaic device stability. *J. Mater. Chem. A* **2018**, *6* (20), 9604−9612.

(21) Cao, J. P.; Yan, F. Recent progress in tin-based perovskite solar cells. *Energy Environ. Sci.* **2021**, *14* (3), 1286−1325.

(22) Xu, L. G.; Feng, X. Y.; Jia, W. B.; Lv, W. X.; Mei, A. Y.; Zhou, Y. H.; Zhang, Q.; Chen, R. F.; Huang, W. Recent advances and challenges of inverted lead-free tin-based perovskite solar cells. *Energy Environ. Sci.* **2021**, *14* (8), 4292−4317.

(23) Wang, J.; Uddin, M. A.; Chen, B.; Ying, X.; Ni, Z.; Zhou, Y.; Li, M.; Wang, M.; Yu, Z.; Huang, J. Enhancing photostability of Sn-Pb perovskite solar cells by an alkylammonium pseudo-halogen additive. *Adv. Energy Mater.* **2023**, *13* (15), No. 2204115.

(24) Zhang, Z. F.; Liang, J. H.; Wang, J. L.; Zheng, Y. T.; Wu, X. Y.; Tian, C. C.; Sun, A. X.; Huang, Y.; Zhou, Z.; Yang, Y. J.; et al. DMSO-Free Solvent Strategy for Stable and Efficient Methylammonium-Free Sn-Pb Alloyed Perovskite Solar Cells. *Adv. Energy Mater.* **2023**, *13* (17), No. 2300181.

(25) Wang, J. T.; Yu, Z. H.; Astridge, D. D.; Ni, Z. Y.; Zhao, L.; Chen, B.; Wang, M. R.; Zhou, Y.; Yang, G.; Dai, X. Z.; et al. Carbazole-Based Hole Transport Polymer for Methylammonium-Free Tin-Lead Perovskite Solar Cells with Enhanced Efficiency and Stability. *Acs Energy Letters* **2022**, *7* (10), 3353−3361.

(26) Yu, Z.; Wang, J.; Chen, B.; Uddin, M. A.; Ni, Z.; Yang, G.; Huang, J. Solution-Processed Ternary Tin (II) Alloy as Hole-Transport Layer of Sn-Pb Perovskite Solar Cells for Enhanced Efficiency and Stability. *Adv. Mater.* **2022**, *34* (49), No. e2205769.

(27) Yang, F. J.; MacQueen, R. W.; Menzel, D.; Musiienko, A.; Al-Ashouri, A.; Thiesbrummel, J.; Shah, S. H.; Prashanthan, K.; Abou-Ras, D.; Korte, L.; et al. Rubidium Iodide Reduces Recombination Losses in Methylammonium-Free Tin-Lead Perovskite Solar Cells. *Adv. Energy Mater.* **2023**, *13* (19), No. 2204339.

(28) Meng, R.; Li, C.; Yang, L.; Li, Z. H.; Wan, Z.; Shi, J. S.; Li, Z. Solvent bath annealing-induced liquid phase Ostwald ripening enabling efficient and stable perovskite solar cells. *J. Mater. Chem. A* **2023**, *11* (9), 4780−4788.

https://doi.org/10.1021/acsenergylett.3c02426
ACS Energy Lett. 2024, 9, 432−441

(29) Zhong, H.; Liu, X.; Liu, M.; Yin, S.; Jia, Z.; Fu, G.; Yang, S.; Kong, W. Suppressing the crystallographic disorders induced by excess PbI2 to achieve trade-off between efficiency and stability for PbI2-rich perovskite solar cells. *Nano Energy* **2023**, *105*, No. 108014.
(30) Macpherson, S.; Doherty, T. A. S.; Winchester, A. J.; Kosar, S.; Johnstone, D. N.; Chiang, Y. H.; Galkowski, K.; Anaya, M.; Frohna, K.; Iqbal, A. N.; et al. Local nanoscale phase impurities are degradation sites in halide perovskites. *Nature* **2022**, *607* (7918), 294−300. From NLM PubMed-not-MEDLINE
(31) Masi, S.; Gualdrón-Reyes, A. F.; Mora-Seró, I. Stabilization of Black Perovskite Phase in FAPbI and CsPbI. *Acs Energy Letters* **2020**, *5* (6), 1974−1985.
(32) Liu, J.; Wang, G.; Song, Z.; He, X. L.; Luo, K.; Ye, Q. Y.; Liao, C.; Mei, J. FAPbSnI mixed metal halide perovskites with improved light harvesting and stability for efficient planar heterojunction solar cells. *J. Mater. Chem. A* **2017**, *5* (19), 9097−9106.
(33) Bu, T.; Li, J.; Li, H.; Tian, C.; Su, J.; Tong, G.; Ono, L. K.; Wang, C.; Lin, Z.; Chai, N.; et al. Lead halide-templated crystallization of methylamine-free perovskite for efficient photovoltaic modules. *Science* **2021**, *372* (6548), 1327−1332. From NLM PubMed-not-MEDLINE
(34) Huerta Hernandez, L.; Haque, M. A.; Sharma, A.; Lanzetta, L.; Bertrandie, J.; Yazmaciyan, A.; Troughton, J.; Baran, D. The role of A-site composition in the photostability of tin−lead perovskite solar cells. *Sustain Energ Fuels* **2022**, *6* (20), 4605−4613.
(35) Chang, Z.; Zheng, D. X.; Zhao, S.; Wang, L.; Wu, S. J.; Liu, L.; Li, Z. P.; Zhang, L.; Dong, Q. S.; Wang, H.; et al. Designing Heterovalent Substitution with Antioxidant Attribute for High-Performance Sn-Pb Alloyed Perovskite Solar Cells. *Adv. Funct. Mater.* **2023**, *33* (22), No. 2214983.
(36) Yu, Z.; Chen, X.; Harvey, S. P.; Ni, Z.; Chen, B.; Chen, S.; Yao, C.; Xiao, X.; Xu, S.; Yang, G.; et al. Gradient Doping in Sn-Pb Perovskites by Barium Ions for Efficient Single-Junction and Tandem Solar Cells. *Adv. Mater.* **2022**, *34* (16), No. e2110351. From NLM PubMed-not-MEDLINE
(37) Jiang, T.; Xu, X.; Lan, Z.; Chen, Z.; Chen, X.; Liu, T.; Huang, S.; Yang, Y. Efficient MA-free Pb-Sn alloyed low-bandgap perovskite solar cells via surface passivation. *Nano Energy* **2022**, *101*, No. 107596.
(38) Flatken, M. A.; Radicchi, E.; Wendt, R.; Buzanich, A. G.; Härk, E.; Pascual, J.; Mathies, F.; Shargaieva, O.; Prause, A.; Dallmann, A.; et al. Role of the Alkali Metal Cation in the Early Stages of Crystallization of Halide Perovskites. *Chem. Mater.* **2022**, *34* (3), 1121−1131.
(39) Rodríguez-Romero, J.; Sanchez-Diaz, J.; Echeverría-Arrondo, C.; Masi, S.; Esparza, D.; Barea, E. M.; Mora-Seró, I. Widening the 2D/3D Perovskite Family for Efficient and Thermal-Resistant Solar Cells by the Use of Secondary Ammonium Cations. *ACS Energy Letters* **2020**, *5* (4), 1013−1021.
(40) Sanchez-Diaz, J.; Sanchez, R. S.; Masi, S.; Krecmarova, M.; Alvarez, A. O.; Barea, E. M.; Rodriguez-Romero, J.; Chirvony, V. S.; Sanchez-Royo, J. F.; Martinez-Pastor, J. P.; Mora-Sero, I. Tin perovskite solar cells with > 1,300 h of operational stability in N(2) through a synergistic chemical engineering approach. *Joule* **2022**, *6* (4), 861−883. From NLM PubMed-not-MEDLINE
(41) Lanzetta, L.; Webb, T.; Zibouche, N.; Liang, X.; Ding, D.; Min, G.; Westbrook, R. J. E.; Gaggio, B.; Macdonald, T. J.; Islam, M. S.; Haque, S. A. Degradation mechanism of hybrid tin-based perovskite solar cells and the critical role of tin (IV) iodide. *Nat. Commun.* **2021**, *12* (1), 2853. From NLM PubMed-not-MEDLINE
(42) Turren-Cruz, S. H.; Saliba, M.; Mayer, M. T.; Juárez-Santiesteban, H.; Mathew, X.; Nienhaus, L.; Tress, W.; Erodici, M. P.; Sher, M. J.; Bawendi, M. G.; et al. Enhanced charge carrier mobility and lifetime suppress hysteresis and improve efficiency in planar perovskite solar cells. *Energy Environ. Sci.* **2018**, *11* (1), 78−86.
(43) Saliba, M.; Matsui, T.; Domanski, K.; Seo, J. Y.; Ummadisingu, A.; Zakeeruddin, S. M.; Correa-Baena, J. P.; Tress, W. R.; Abate, A.; Hagfeldt, A.; Gratzel, M. Incorporation of rubidium cations into perovskite solar cells improves photovoltaic performance. *Science* **2016**, *354* (6309), 206−209. From NLM PubMed-not-MEDLINE
(44) Reshmi Varma, P. C. Low-Dimensional Perovskites. In *Perovskite Photovoltaics*; Thomas, S., Thankappan, A., Eds.; Academic Press, 2018; pp 197−229.
(45) Kirmani, A. R.; Ostrowski, D. P.; VanSant, K. T.; Byers, T. A.; Bramante, R. C.; Heinselman, K. N.; Tong, J. H.; Stevens, B.; Nemeth, W.; Zhu, K.; et al. Metal oxide barrier layers for terrestrial and space perovskite photovoltaics. *Nature Energy* **2023**, *8* (2), 191.
(46) Li, M.; Zuo, W.-W.; Yang, Y.-G.; Aldamasy, M. H.; Wang, Q.; Cruz, S. H. T.; Feng, S.-L.; Saliba, M.; Wang, Z.-K.; Abate, A. Tin Halide Perovskite Films Made of Highly Oriented 2D Crystals Enable More Efficient and Stable Lead-free Perovskite Solar Cells. *ACS Energy Letters* **2020**, *5* (6), 1923−1929.
(47) Xia, J.; Sohail, M.; Nazeeruddin, M. K. Efficient and Stable Perovskite Solar Cells by Tailoring of Interfaces. *Adv. Mater.* **2023**, *35* (31), No. e2211324. From NLM PubMed-not-MEDLINE
(48) Degani, M.; An, Q.; Albaladejo-Siguan, M.; Hofstetter, Y. J.; Cho, C.; Paulus, F.; Grancini, G.; Vaynzof, Y. 23.7% Efficient inverted perovskite solar cells by dual interfacial modification. *Sci. Adv.* **2021**, *7*, eabj7930.
(49) Kapil, G.; Bessho, T.; Maekawa, T.; Baranwal, A. K.; Zhang, Y.; Kamarudin, M. A.; Hirotani, D.; Shen, Q.; Segawa, H.; Hayase, S. Tin-Lead Perovskite Fabricated via Ethylenediamine Interlayer Guides to the Solar Cell Efficiency of 21.74%. *Adv. Energy Mater.* **2021**, *11* (25), No. 2101069.
(50) Hu, S.; Otsuka, K.; Murdey, R.; Nakamura, T.; Truong, M. A.; Yamada, T.; Handa, T.; Matsuda, K.; Nakano, K.; Sato, A.; et al. Optimized carrier extraction at interfaces for 23.6% efficient tin−lead perovskite solar cells. *Energy Environ. Sci.* **2022**, *15* (5), 2096−2107.
(51) Yoo, S. M.; Yoon, S. J.; Anta, J. A.; Lee, H. J.; Boix, P. P.; Mora-Seró, I. An Equivalent Circuit for Perovskite Solar Cell Bridging Sensitized to Thin Film Architectures. *Joule* **2019**, *3* (10), 2535−2549.
(52) Riquelme, A. J.; Valadez-Villalobos, K.; Boix, P. P.; Oskam, G.; Mora-Sero, I.; Anta, J. A. Understanding equivalent circuits in perovskite solar cells. Insights from drift-diffusion simulation. *Phys. Chem. Chem. Phys.* **2022**, *24* (26), 15657−15671. From NLM PubMed-not-MEDLINE
(53) Liu, Z.; Li, H.; Chu, Z.; Xia, R.; Wen, J.; Mo, Y.; Zhu, H.; Luo, H.; Zheng, X.; Huang, Z. Reducing Perovskite/C(60) Interface Losses via Sequential Interface Engineering for Efficient Perovskite/Silicon Tandem Solar Cell. *Adv. Mater.* **2023**, e2308370. From NLM Publisher

https://doi.org/10.1021/acsenergylett.3c02426
ACS Energy Lett. 2024, 9, 432−441